

Hydrogen evolution through ammonia borane hydrolysis over iron tailored pig manure catalyst

*Original*

Hydrogen evolution through ammonia borane hydrolysis over iron tailored pig manure catalyst / Gianola, Giulia; Bartoli, Mattia; Pirri, Candido; Bocchini, Sergio. - In: INTERNATIONAL JOURNAL OF HYDROGEN ENERGY. - ISSN 1879-3487. - (2024), pp. 1-8. [10.1016/j.ijhydene.2023.10.202]

*Availability:*

This version is available at: 11583/2983854 since: 2023-11-15T00:08:58Z

*Publisher:*

Elsevier

*Published*

DOI:10.1016/j.ijhydene.2023.10.202

*Terms of use:*

This article is made available under terms and conditions as specified in the corresponding bibliographic description in the repository

*Publisher copyright*

(Article begins on next page)



Contents lists available at ScienceDirect

## International Journal of Hydrogen Energy

journal homepage: [www.elsevier.com/locate/he](http://www.elsevier.com/locate/he)

# Hydrogen evolution through ammonia borane hydrolysis over iron tailored pig manure catalyst

Giulia Gianola<sup>a,b</sup>, Mattia Bartoli<sup>b,c,\*</sup>, Candido Fabrizio Pirri<sup>a,b</sup>, Sergio Bocchini<sup>a,b</sup><sup>a</sup> Department of Applied Science and Technology, Politecnico di Torino, Corso Duca Degli Abruzzi, 24, 10129, Torino, Italy<sup>b</sup> Center for Sustainable Future Technologies (CSFT), Istituto Italiano di Tecnologia (IIT), Via Livorno, 60, 10144, Torino, Italy<sup>c</sup> Consorzio Interuniversitario Nazionale per la Scienza e Tecnologia dei Materiali (INSTM), Via G. Giusti 9, 50121, Florence, Italy

## ARTICLE INFO

Handling editor: Dr. E.A. Veziroglu

## Keywords:

Ammonia borane

Hydrogen storage

Pig manure

Hydrogen evolution

Hydrolysis

## ABSTRACT

Hydrogen storage systems have become of great interest particularly especially for those that conjugate a high storage capacity together with high safety standards. Chemical storage using amino borane has attracted a great interest and ammonia borane is playing a major role in the field due to the hydrogen storage capacity up to 19 wt%. Nevertheless, the hydrogen evolution from ammonia borane is a matter of great complexity and hydrolytic methods represent the simpler way to approach it. Actually, the ammonia borane hydrolysis is carried out by using complex catalysts not containing critical raw materials and/or noble metals. In the present work, we report the production of iron based heterogeneous catalyst support onto carbonized pig manure. The complexity of this waste stream was very helpfully to provide an active surface for the anchoring of iron nanoparticles and promoting the hydrogen evolution from hydrolysis of ammonia borane reaching a conversion of 98.3% at 50 °C with an iron loading of 10 wt%. The catalytic system reduced the activation energy of the reaction up to 51% increasing the kinetic constant of the reaction of one order of magnitude. Furthermore, the stability of the catalytic system was preserved after three cycles without appreciable changes.

## 1. Introduction

In the current era, energy resources are becoming increasingly scarce, posing significant challenges to the environment's quality and overall health [1]. To address this issue, numerous initiatives have been deployed with the ambitious goal of completely transitioning away from fossil fuels and establishing a carbon-negative society in the coming decades [2]. This paradigm shift envisions a transitional period where various eco-friendly energy sources and vectors will lead the way towards a sustainable society [3]. Among the promising approaches to achieve a carbon-negative production network, the hydrogen-based economy stands out, especially when considering technologies capable of producing green and blue hydrogen [4]. However, the widespread adoption of a hydrogen-based economy faces two critical challenges: efficient hydrogen production and safe storage. Regarding hydrogen production, intense research has been dedicated to improving production systems, resulting in significant advances in advancements in sustainable production through electrolyzers [5–7]. Nevertheless, the hydrogen storage still remains a major unsolved issue in the field [8]. Currently, large hydrogen volumes are stored as liquid hydrogen in

expensive insulated vessels, which can lead to product losses due to accidental spill and evaporation limiting to those applications that require high volume and pure gas under strictly controlled conditions such as chemical and aerospace industries [9].

Expanding the use of hydrogen beyond industrial sectors needs alternative storage technology that fulfill stringent safety requirements [10] and exhibit high gravimetric specific capacity [11]. While physisorbed approach based on porous materials (i.e. metal/chemical organic frameworks [12–14], inorganics [15], carbon [16]) offer a reasonable safety, they are restricted by the Chahine rule, which limits to 1 wt% of adsorbed hydrogen per 500 m<sup>2</sup>/g of surface area [17] and require low temperature for storage.

Alternatively, chemical hydrogen storage routes offer promising solution, yielding storage material with high gravimetric specific capacity in compounds such as ammonia [18] or methane [19]. However, this method requires high release temperature.

A more promising and facile chemical hydrogen storage pathway involves the use of species such as ammonia borane (AB), which can release hydrogen through thermolysis or hydrolysis [20]. AB can reach a remarkable 19.6 wt% value of high theoretical gravimetric hydrogen

\* Corresponding author. Center for Sustainable Future Technologies (CSFT), Istituto Italiano di Tecnologia (IIT), Via Livorno, 60, 10144, Torino, Italy.

E-mail address: [mattia.bartoli@iit.it](mailto:mattia.bartoli@iit.it) (M. Bartoli).

<https://doi.org/10.1016/j.ijhydene.2023.10.202>

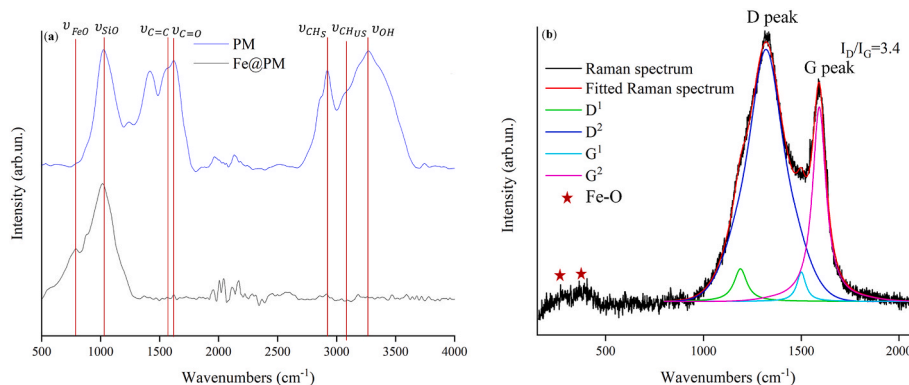
Received 5 September 2023; Received in revised form 12 October 2023; Accepted 20 October 2023

0360-3199/© 2023 Published by Elsevier Ltd on behalf of Hydrogen Energy Publications LLC.

**Table 1**

TGA program used for the evaluation of proximate analysis of PM and Fe@PM

|         | Starting temperature (°C) | Ending temperature (°C) | Hold time at ending temperature (min) | Heating rate (°C min <sup>-1</sup> ) | Atmosphere     |
|---------|---------------------------|-------------------------|---------------------------------------|--------------------------------------|----------------|
| 1° step | 30                        | 110                     | 30                                    | 20                                   | N <sub>2</sub> |
| 2° step | 110                       | 950                     | 7                                     | 20                                   | N <sub>2</sub> |
| 3° step | 950                       | 760                     | 60                                    | 20                                   | Air            |

a) Constant flux of carrier and protective gas of 20 mL min<sup>-1</sup>**Fig. 1.** Spectroscopic investigation through a) FT-IR (ATR mode) of PM (blue line) and Fe@PM (black line) and through b) Raman spectroscopy of Fe@PM in the region from 250 up to 2200 cm<sup>-1</sup>. (For interpretation of the references to colour in this figure legend, the reader is referred to the Web version of this article.)**Table 2**

Proximate analysis of PM and Fe@PM calculated in according with Torquato et al. [46].

| Sample | Proximate analysis |             |                     |            |
|--------|--------------------|-------------|---------------------|------------|
|        | Moisture (wt.%)    | VOCs (wt.%) | Fixed carbon (wt.%) | Ash (wt.%) |
| PM     | 1.5                | 34.8        | 39.1                | 24.6       |
| Fe@PM  | 0.7                | 12.5        | 32.4                | 54.4       |

**Table 3**

EDX analysis of fresh Fe@PM and Fe@PM after three catalytic cycles.

| Elements | Fe@PM (wt.%) | Fe@PM after three catalytic cycles (wt.%) |
|----------|--------------|---|
| C        | 37.3         | 34.5                                      |
| O        | 23.3         | 24.3                                      |
| Na       | 0.3          | 1.2                                       |
| Mg       | 0.4          | 0.6                                       |
| Al       | 1.0          | 1.1                                       |
| Si       | 0.8          | 1.2                                       |
| P        | 1.9          | 1.1                                       |
| S        | 2.3          | 3.1                                       |
| Cl       | 0.5          | 0.6                                       |
| Ca       | 7.6          | 6.4                                       |
| Fe       | 24.5         | 25.9                                      |

storage capacity up the remarkable. While thermolysis of AB involves several complex pathways with the release of complex species [21], AB hydrolysis stand up for its simplicity, requiring only water as additional reagent. Various catalytic routes have been explored for AB hydrolysis, including ionic liquids [22–24], porous materials [25,26] and nanostructured supported catalysts [27,28]. Among these option, nanostructured supported catalysts are particularly intriguing due to exceptional performance and ease of recyclability, although they are often based on complex textured materials (i.e. carbon nanotubes [29], graphene oxide [30]) containing critical raw materials (e.g. cobalt [31], platinum [32], palladium [33], ruthenium [34], rhodium [35]).

Recent research efforts have focused on developing effective catalyst based on non critical raw materials [36] potentially exploiting waste-streams as sustainable sources [37,38]. In the present work, we present the development of an iron tailored carbonized pig manure (Fe@PM) as

an efficient hydrogen evolution through ammonia borane hydrolysis. Pig manure (PM) management contributes significantly to greenhouse gas emissions, accounting for up to 18 % total annual emission [39], and contains organic matter [40] and several inorganics such as phosphates, nitrates and chlorides [41]. The complex nature of PM may prove beneficial for the catalyst production as reported by several authors in literature [42]. In this research, we reduced mixed an iron based precursor with pig manure and formed iron based nanostructures using a carbothermal reduction process for the exploitation of hydrogen evolution from ammonia borane water solutions.

## 2. Materials and methods

### 2.1. Materials

Ammonium sulphate (>98 %), Sodium Borohydride (>99 %), Iron (III) nitrate nonahydrate (>98 %) and tetrahydrofuran (>98) were purchased from Sigma Aldrich and used without any further purifications.

PM was provided from local farmers (Piemonte, Italy) and sterilized in autoclave at 120° for 1 h and dried for 72 h at 105°.

### 2.2. Methods

#### 2.2.1. Synthesis

AB was synthesized and purified accordingly with experimental procedure reported by Ramachandran et al. [43].

Fe@PM was produced according to Tamborrino et al. [44]. 50 g of dried PM was suspended in 250 mL of deionized water together iron nitrate with a weight ration of Fe/PM of 1:10 (considering the PM without the its ash content). The mixture was stirred for 10 min and dried in a ventilated oven at 105 °C overnight. The dried material was used without any additional purifications. Fe@PM was prepared through a carbothermal process using a tubular furnace (Carbolite TZF 12/65/550) in nitrogen atmosphere with a heating rate of 10 °C/min and kept at 550 °C for 30 min.

#### 2.2.2. Materials characterization

Fe@PM were preliminary characterized through Fourier

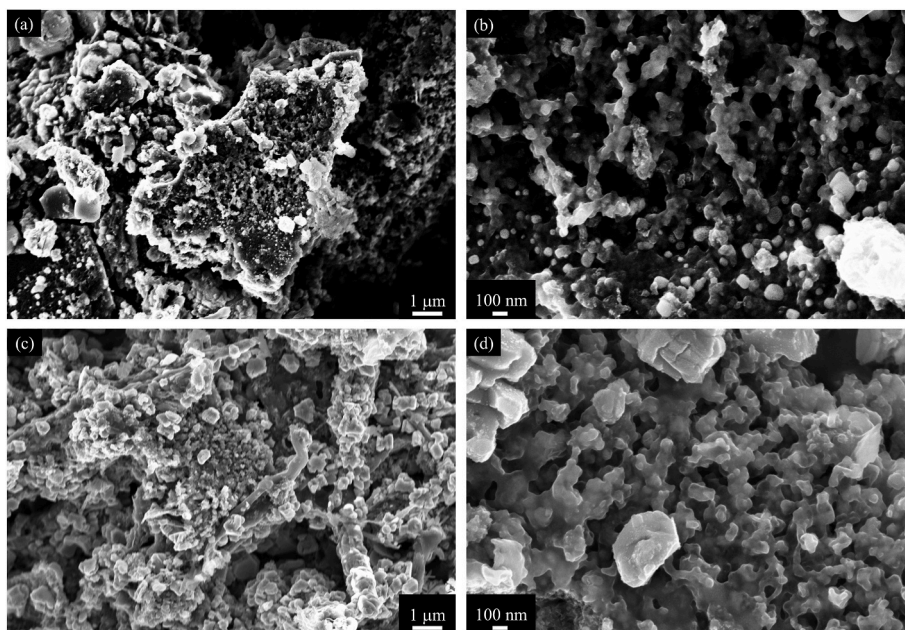


Fig. 2. FESEM captures at different magnifications of fresh a-b) Fe@PM and c-d) Fe@PM after three catalytic cycles.

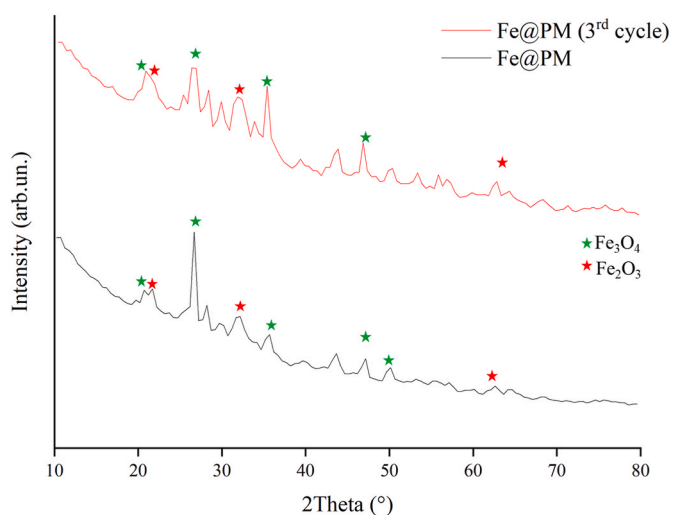


Fig. 3. XRD analysis from 10 to 80° 2Theta Fe@PM (black line) and Fe@PM (red line) after three catalytic cycles. (For interpretation of the references to colour in this figure legend, the reader is referred to the Web version of this article.)

transformed infrared (FT-IR) spectroscopy in the range from 500 to 4000  $\text{cm}^{-1}$  using a spectrometer Nicolet 5700 (ThermoScientific) operated in attenuated total reflectance (ATR) equipped with a diamond window (Smartorbit, ThermoScientific) and through Raman spectroscopy using a Renishaw inVia (H43662 model, Gloucestershire, UK) equipped with a green laser line (532 nm) and a 50 $\times$  objective. Raman spectrum was collected from 250 to 4000  $\text{cm}^{-1}$  and D and G peaks were fitted by using the protocol reported by Tagliaferro et al. [45].

Fe@PM specific surface area was measured through  $\text{N}_2$  sorption at 196 °C on a micromeritics Tristar II instrument (Micromeritics Instrument Corporation, USA) using the Langmuir model.

XRD analyses were performed by using Panalytical X'PERT PRO PW3040/60 diffractometer (Cu K $\alpha$  radiation at 40 kV and 40 mA, Panalytical BV, Almelo, The Netherlands). The diffraction spectra were obtained from biochar powder in the  $2\theta$  range from 10 to 80° with a step size of 0.013°. XRD spectra were analysed by using freeware software

QualX software. Only species with a quality match of 80 % or higher were reported.

Proximate analysis of PM and Fe@PM were carried out accordingly with the procedure reported by Torquato et al. [46] using thermogravimetric analysis (TGA) using a TG 209F1 Libra a three step program as reported in Table 1.

The weight loss of the first step is due to the release of moisture, the weight loss of the second step is due to the volatile organic matter (VOCs) and the weight loss of the last step is the fixed carbon. The residue amount after the third step is the total ash content.

Surface functionalities and atomic species oxidation states of Fe@PM were investigated through X-ray photoelectron spectroscopy (XPS) using a X-ray photoelectron spectrometer PHI 5000 Versaprobe Physical Electronics (Chanhassen, MN, USA) and a monochromatic Al K- $\alpha$  X-ray source with 1486.6 eV energy, 15 kV voltage, and 1 mA anode current. High resolved spectra of C1s, O1s and Fe2p were fitted by using Gaussian lineshape for each component and a Shirley line for the baseline. We used a Levenberg-Marquardt algorithm for the fit and obtaining uncertainties of up  $\pm 1$  % for each components [47,48].

The morphology and elemental analysis of Fe@PM were investigated using a Field Emission Scanning Electrical microscope (FE-SEM) Zeiss SupraTM 25 (Oberkochen, Germany) equipped with an energy dispersive X-ray detector (EDX, Oxford Inca Energy 450, Oberkochen, Germany).

### 2.2.3. AB hydrolytic test for hydrogen evolution

AB hydrolysis was carried out at different temperatures (30, 40 and 50 °C) in nitrogen atmosphere. Fe@PM was put in a two-necked round-bottom flask connected to a gas burette and another to an addition pressure-equalized funnel. Fe@PM was stirred at 300 rpm for 10 min and AB was added reaching a final concentration of up 0.5 M. and a AB/Fe ratio of 0.0, 5.0 and 10.0 wt%. The hydrogen evolution was monitored using the gas burette considering the external pressure and temperature. After the reaction was ended the catalyst was recovered by filtration, dried at 50 °C and 20 mbar until constant weight prior to be reused and characterized. Each catalytic test was run twice without observing detectable changes in the conversion results.

Kinetic constants (k) for each reaction were obtained by fitting the conversion vs time plot using a pseudo first order model as reported by Abutaleb et al. [49] and activation energies ( $\Delta G_a$ ) were calculated by

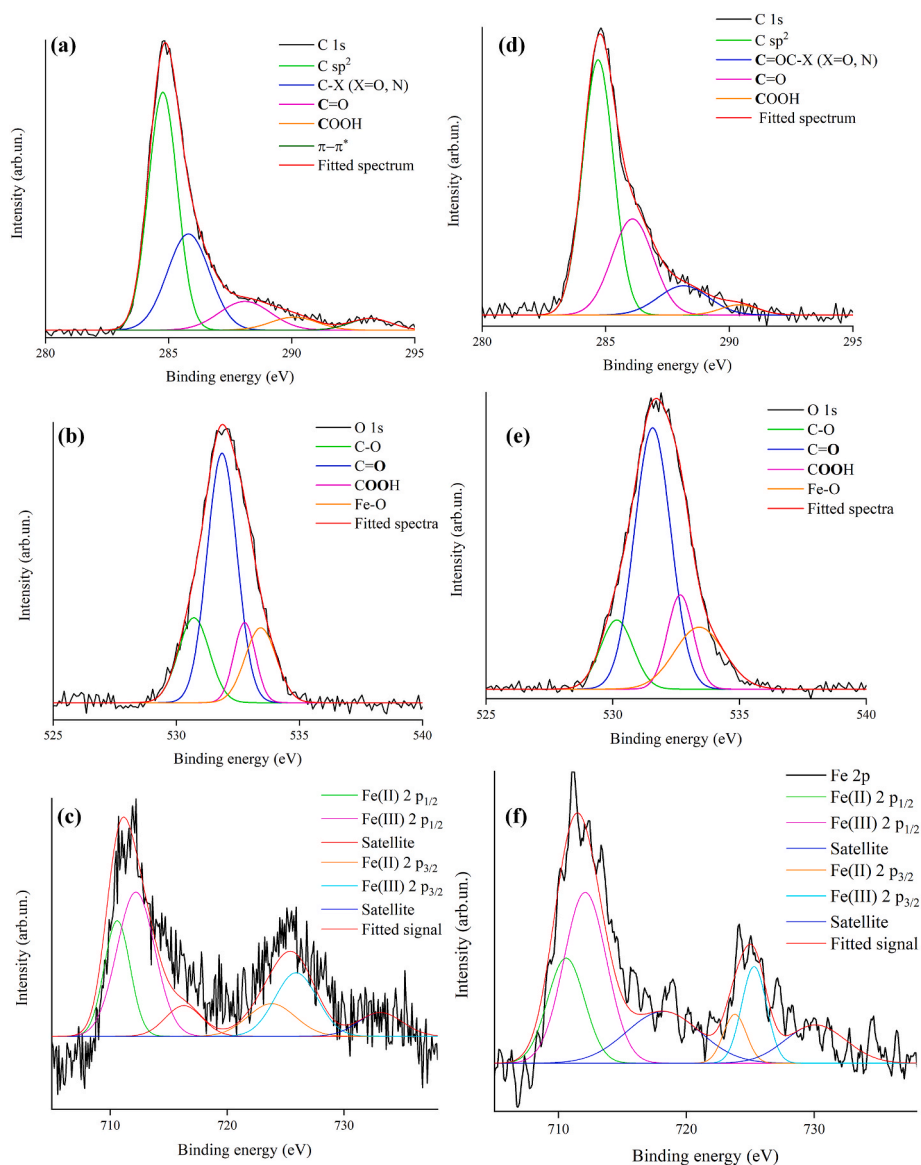


Fig. 4. XPS analysis (C1s, O1s, Fe 2p) of a-c) Fe@PM and d-f) Fe@PM of after three catalytic cycles.

Table 4

Chemical functionalities distribution obtained from XPS analysis of C1s, O1s and Fe 2p) spectra.

| Chemical functionalities <sup>a</sup> |          | Fe@PM (%) | Fe@PM after three catalytic cycles (%) |
|---------------------------------------|----------|-----------|--|
| Carbon                                | C $sp^2$ | 53        | 58                                     |
|                                       | C-O      | 31        | 29                                     |
|                                       | C=O      | 11        | 11                                     |
|                                       | COOH     | 5         | 3                                      |
|                                       |          |           |  |
| Oxygen                                | C-O      | 19        | 13                                     |
|                                       | C=O      | 53        | 55                                     |
|                                       | COOH     | 12        | 14                                     |
|                                       | Fe-O     | 17        | 18                                     |
| Iron                                  | Fe (II)  | 40        | 41                                     |
|                                       | Fe(III)  | 60        | 59                                     |
|                                       |          |           |  |

<sup>a</sup> Uncertainty of  $\pm 1$  %.

using Arrhenius equation [50].

### 3. Results

#### 3.1. Characterization of the catalysts

PM is a complex feedstock but as reported by Saeys et al [51], with a quite regular inorganic composition. The preliminary characterization of the materials was run by spectroscopic methods as reported in Fig. 1.

As reported in Fig. 1 a, the FT-IR spectrum of PM showed a material still rich in organic matter with broad bands centered at 3275, 3160, 2937  $\text{cm}^{-1}$  respectively due to  $\nu_{\text{OH}}$ , and unsaturated and saturated  $\nu_{\text{CH}}$ . The presence of unsaturated compounds was also supported by the broad  $\nu_{\text{C}=\text{C}}$  band centered at 1656  $\text{cm}^{-1}$  while the presence hydroxyl function was confirmed by the  $\nu_{\text{C}-\text{O}}$  centered at 1218  $\text{cm}^{-1}$ . The FT-IR spectrum of Fe@PM was considerably simpler than the previous one showing only a broad band centered at 1021  $\text{cm}^{-1}$  due to the hydroxyl residues contained into the carbonized PM structure. Furthermore, the presence of the peak centered at 779  $\text{cm}^{-1}$  ( $\nu_{\text{FeO}}$ ) proved the presence of iron oxide formation in Fe@PM as reported in literature [52]. Raman spectrum of Fe@PM (Fig. 1 b) allowed us to evaluate the organization of

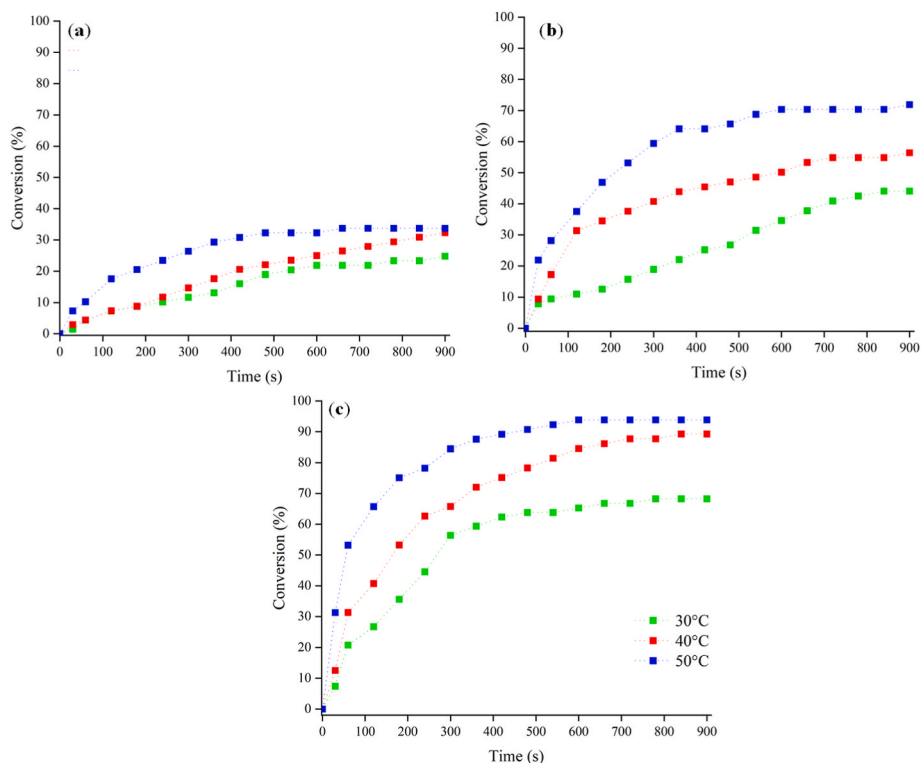


Fig. 5. Hydrogen evolution test with a loading of Fe of a) 0 wt%, b) 5 wt% and c) 10 wt%. Fe loading is calculated based on EDX analysis.

Table 5

Values of  $k$  and  $\Delta G_a$  of hydrolysis of AB under different loading of iron.

| Fe loading (wt.%) | $k$ ( $s^{-1}$ )    |                     |                      | $\Delta G_a$ (kJ/mol) |
|-------------------|---------------------|---------------------|----------------------|-----------------------|
|                   | 30 °C               | 40 °C               | 50 °C                |                       |
| 0                 | $0.7 \cdot 10^{-3}$ | $0.9 \cdot 10^{-3}$ | $4.0 \cdot 10^{-3}$  | 111                   |
| 5                 | $1.0 \cdot 10^{-3}$ | $3.0 \cdot 10^{-3}$ | $6.0 \cdot 10^{-3}$  | 84                    |
| 10                | $5.0 \cdot 10^{-3}$ | $7.0 \cdot 10^{-3}$ | $20.0 \cdot 10^{-3}$ | 54                    |

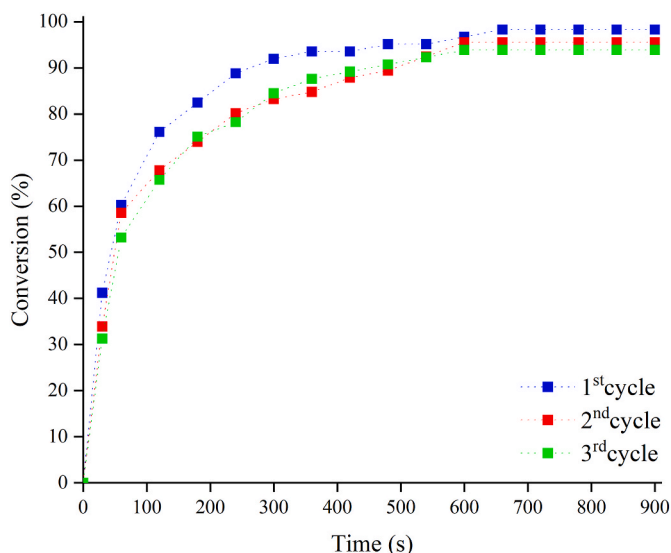


Fig. 6. Hydrogen evolution test with a loading of Fe up to 10 wt% during three catalytic cycles run at 50 °C. Fe loading is calculated based on EDX analysis.

graphitic carbon formed during the carbothermal reduction process through the estimation of both intensity ratio of the D and G bands ( $I_D/I_G$  ratio) [40] and the average length of graphitic clusters diameter ( $L_a$ ) [53]. The D peak centered at  $1322 \text{ cm}^{-1}$  was quite broad compared to G peak centered at  $1591 \text{ cm}^{-1}$  with a resulting  $I_D/I_G$  ratio up to 3.4. This value is quite high and suggest the presence of highly disorganized carbon matrix [44,54–59]. Accordingly, the average value of  $L_a$  is up to  $13 \text{ \AA}$  and it is quite low confirming the poor reduced graphitization degree of carbon formed at  $550 \text{ }^\circ\text{C}$ . Furthermore, the presence of small broad peaks at  $274$  and  $383 \text{ cm}^{-1}$  supports the presence of ferrite on the surface of Fe@PM as reported by Yew et al. [60] promoted by the partial reduction of Fe(III) precursors [61–63].

The proximate analysis reported in Table 2 showed a quite high amount of ash in both PM and Fe@PM with value respectively of up to 24.6 and 54.4 wt%. The increment of ash noticed for Fe@PM was due to the carbothermal process that involved the reduction of iron precursors with the oxidation of organic matter as clearly proved by the concurrent decrement of VOCs and fixed carbon. This allowed to reduced the variability promoted by the presence of organic structure that survived from the thermal conversion (see Table 3).

Additionally, Fe@PM showed a specific surface area up to  $55 \text{ m}^2/\text{g}$  and a total pore volume  $0.04 \text{ cm}^3/\text{g}$ .

The morphological analysis of Fe@PM (Fig. 2 a-b) showed an organic matrix composed by high chunks of up  $10 \text{ }\mu\text{m}$  (Fig. 2 a) decorated with iron based inorganic particles of up around  $80\text{--}100 \text{ nm}$  (Fig. 2b). As reported in Table 2, the amount of iron inserted through the carbothermal process reach up to 24.5 wt% and several inorganic species were detected in according with the complex composition of PM [64]. As reported by Kalindi et al. [65], the inorganic impurities can boost the hydrogen evolution from AB in hydrolytic condition promoting especially the acidic sites such those formed by aluminum or iron oxide [66, 67].

As reported in Fig. 3, XRD spectrum of Fe@PM showed the reflection of both  $\text{Fe}_3\text{O}_4$  and  $\text{Fe}_2\text{O}_3$  with a ratio of close to 4:1 together with plenty of other peak due to the inorganic alkaline salts (i.e. phosphates,

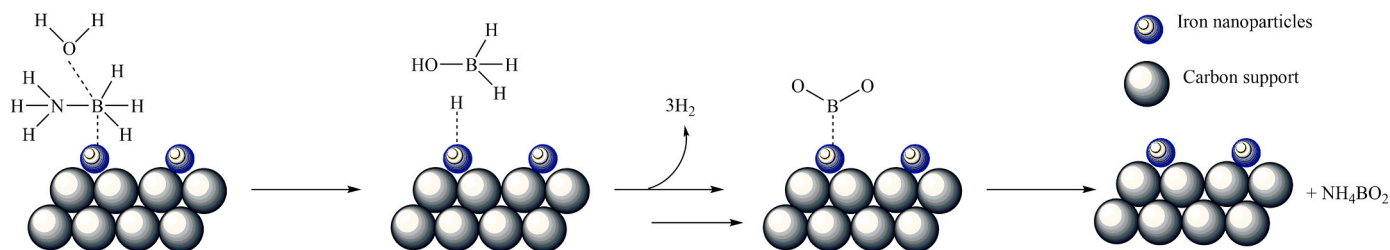


Fig. 7. Hypothetical mechanism of AB hydrolysis over Fe@PM.

Table 6

Comparison between catalytic performance of Fe@PM and the alternative catalytic systems.

| Catalyst                                     | Particle size (nm) | Conversion <sup>a</sup> (%) | Conversion (%) | t (min) | $\Delta G_a$ (kJ/mol) | Catalyst loading (wt.%) | Reference    |
|--|--------------------|-----------------------------|----------------|---------|-----------------------|-------------------------|--------------|
| Fe@PM  | 80                 | 97                          | 2.9            | 15      | 54                    | 10                      | Present work |
| Co/ $\gamma$ -Al <sub>2</sub> O <sub>3</sub> | 13                 | 97                          | 2.9            | 70      | 62                    | 10                      | [74]         |
| Fe nanoparticles                             | 60                 | ~100                        | 3              | 8       | Not reported          | 12                      | [75]         |
| Ni nanoparticles                             | <19                | ~100                        | 3              | 6       | Not reported          | 10                      | [76]         |
| Cu@zeolite                                   | 50                 | ~100                        | 3              | 120     | 54                    | 2                       | [77]         |
| Ru/ $\gamma$ -Al <sub>2</sub> O <sub>3</sub> | 2                  | ~100                        | 3              | 3       | 23                    | 2                       | [78]         |
| Rh/ $\gamma$ -Al <sub>2</sub> O <sub>3</sub> | 3                  | ~100                        | 3              | 2       | 21                    | 2                       | [78]         |
| Pt/ $\gamma$ -Al <sub>2</sub> O <sub>3</sub> | 2                  | ~100                        | 3              | 1       | 21                    | 2                       | [78]         |
| Ru@Zeolite                                   | 1                  | ~100                        | 3              | 8       | 67                    | 0.5                     | [79]         |

<sup>a</sup>) Conversion = 100\*( $n_{H_2}$  produced)/(theoretical  $n_{H_2}$ ), where theoretical  $n_{H_2}$  = 3 mol.

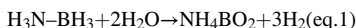
silicates, chlorides) include in the carbon matrix in agreement with the elemental composition reported in Table 2. It was also observed a big bump of the signal up to 27° due to the massive presence of amorphous carbon produced after the carbothermal reduction [68].

A further investigation of iron oxidation states and surface texture was carried out through XPS analysis as reported in Fig. 4 and summarized in Table 4.

As shown in Fig. 4 c, the Fe 2p spectrum showed only two components due to Fe (II) ( $2p_{1/2}$  710.7 eV,  $2p_{3/2}$  723.7 eV) and Fe(III) ( $2p_{1/2}$  711.9,  $2p_{3/2}$  725.6 eV) with a ratio of around 1.5 supporting the presence of a large amount of Fe<sub>3</sub>O<sub>4</sub> and around 20 wt% Fe<sub>2</sub>O<sub>3</sub>. C1s spectrum (Fig. 4 a) showed the absence of C sp<sup>3</sup> and the presence of large amount of C sp<sup>2</sup> up to 53 % centered at 285.7 eV supporting carbonization of PM. The large amount of oxygen presented ranging from hydroxyl to carboxylic functionalities suggest a large tailoring of carbon formed even after the carbothermal reduction of iron.

### 3.2. Catalytic tests

Hydrolysis of AB sketched in eq.1 is a selective reaction producing up to 3 mol for each mole of AB consumed with a mechanism proceeding through the addition of two molecules of water and the formation of highly reactive boron species [69].



In the present work, we studied the hydrogen evolution from ammonia borane hydrolysis at temperature from 30 °C up to 50 °C with an iron loading ranging 0 up to 10 wt% as reported in Fig. 5 evaluating both k and  $\Delta G_a$  as summarized in Table 5.

As reported in in Fig. 5 a, the non-catalysed hydrolysis of AB involved a slow and low release of hydrogen reaching up a maximum conversion of up to 17.8 % at 30 °C after 900 s. An appreciable increment was observed by increasing the temperature up to 40 and 50 °C with conversion values up to 32.2 % and 33.3 %. The increment of reaction temperature positively also affected k that reached up  $4.0 \cdot 10^{-3} \text{ s}^{-1}$  at 50 °C. As show in Fig. 5 b, the addition of Fe@PM with a Fe loading of up to 5 wt% improved the hydrogen evolution reaching up to 71.9 % at 50 °C and increment of k from  $1.0 \cdot 10^{-3} \text{ s}^{-1}$  at 30 °C up to  $6.0 \cdot 10^{-3}$  with

an increment over the double compared to the non-catalysed reaction. A further increment of iron loading up to 10 wt% (Fig. 5 c) promote a further boost of conversion reaching up to 68.7 % at 30 °C with a k of up to  $5.0 \cdot 10^{-3} \text{ s}^{-1}$  while and increment of temperature induced greater enhancements compared with the other test reaching a conversion of up 98.3 % and a k  $20.0 \cdot 10^{-3} \text{ s}^{-1}$ . The positive effect of the catalyst was proved by the decrement of  $\Delta G_a$  from 111 down to 54 kJ/mol using an iron loading of 10 wt% suggesting a reaction mechanism as the one reported by Wu et al. [69] based on the coordination and hydrolytic decomposition of AB over the metal oxide nanosurfaces with adsorption and desorption process as summarized in Fig. 7.

It is particularly relevant observing the crucial role of the defect of oxygen on the surface of catalyst in the AB hydrolysis as reported by several authors [70,71]. This is key strong point of Fe@PM compared on highly organized materials [72,73].

As shown in Fig. 6, the catalytic systems showed a good stability upon up to 3 cycles at 50 °C using an iron loading of up to 10 wt% without showing a small decrement of activity down to 93.9 %.

A comprehensive analysis of Fe@PM after three catalytic cycles showed a substantial preservation of shape of nanostructured surface of Fe@PM (Fig. 2 c and d) with a negligible increment of iron content up to 25.9 % reasonably due to the loss of some inorganic salts as proved by the reduction of Ca and P and modification in the XRD spectrum of the recycled catalyst. XPS spectra of recycled catalyst (Fig. 4 d-f) did not show any appreciable differences with a negligible increment of 1 % of Fe (II) upon Fe (III) without observing the presence of Fe (0).

As shown in Table 6, Fe@PM showed a  $\Delta G_a$  comparable with the one achieved by using copper nanoparticles supported on zeolites [77] but considerably higher of the one achievable by using noble metals [78]. Furthermore, noble metals required lower loading but the Fe@PM was able to achieved the same conversions value with very close time. Additionally, Fe@PM outperformed materials such as Co/ $\gamma$ -Al<sub>2</sub>O<sub>3</sub> [74] showing similar result of colloidal iron [75] or nickel [76] nanoparticles eve if with a great time to completion.

### 4. Conclusions

The hydrogen evolution from AB hydrolysis is a topic of significant interest and the development of new catalytic systems has garnered

considerable attention. Utilizing waste pig manure presents a remarkable opportunity to achieve a complex texture of the catalytic support while simultaneously finding an alternative valorization route for challenging-to-manage waste streams. Moreover, the fabrication of Fe@PM involved the use of a non-critical raw material, iron, without compromising the catalyst performances. This results in an impressive conversion rate of up to 98.3 % reducing the  $\Delta G_a$  up to 51 % and increasing the reaction rate over two orders of magnitude, using an iron loading of up to 10 wt%. The stability over three cycles proved the possible utilization of Fe@PM for prolonged utilization without any detectable leaching.

We firmly believe that the valorization of waste streams could represent a solid strategy to create an integration on which the hydrogen economy will grow and proliferate in the society.

### Declaration of competing interest

The authors declare that they have no known competing financial interests or personal relationships that could have appeared to influence the work reported in this paper.

### Acknowledgements

This study was carried out within the Agritech National Research Center and received funding from the European Union Next-GenerationEU (PIANO NAZIONALE DI RIPRESA E RESILIENZA (PNRR) – MISSIONE 4 COMPONENTE 2, INVESTIMENTO 1.4 – D.D. 1032 June 17, 2022, CN00000022). Furthermore, authors wish to thank European Union for the financial support through the Next Generation EU-projects “Nord Ovest Digitale E Sostenibile-NODES” (PNRR, D.D. n.1054 June 23, 2022) and NEST “Network for Energy Sustainable Transition-NEST”(PE0000021, D.D. n.341 March 15, 2022). Author also acknowledges Ministero dello Sviluppo Economico (MISE) and Ministero della Transizione Ecologica (MITE) for the financial support. This manuscript reflects only the authors views and opinions, neither the European Union nor the European Commission can be considered responsible for them.

### References

- Hainsch K, Löffler K, Burandt T, Auer H, del Granado PC, Pisciella P, Zwickl-Bernhard S. Energy transition scenarios: what policies, societal attitudes, and technology developments will realize the EU Green Deal? *Energy* 2022;239: 122067.
- Wolf S, Teitge J, Mielke J, Schütze F, Jaeger C. The European green deal—more than climate neutrality. *Intereconomics* 2021;56:99–107.
- Bairrão D, Soares J, Almeida J, Franco JF, Vale Z. Green hydrogen and energy transition: current state and prospects in Portugal. *Energies* 2023;16:551.
- Lagioia G, Spinelli MP, Amicarelli V. Blue and green hydrogen energy to meet European Union decarbonisation objectives. An overview of perspectives and the current state of affairs. *Int J Hydrogen Energy* 2023;48:1304–22.
- Ishaq H, Dincer I, Crawford C. A review on hydrogen production and utilization: challenges and opportunities. *Int J Hydrogen Energy* 2022;47:26238–64.
- Mohammadi A, Mehropooya M. A comprehensive review on coupling different types of electrolyzer to renewable energy sources. *Energy* 2018;158:632–55.
- Bodner M, Hofer A, Hacker V. H<sub>2</sub> generation from alkaline electrolyzer. *Wiley Interdiscip. Rev.: Energy Environ* 2015;4:365–81.
- Office of Energy Efficiency and Renewable Energy. *Energy. Hydrogen Storage; 2022*. URL, <https://www.hydrogen.energy.gov/program-areas/storage>. [Accessed 4 November 2023].
- Wijayanta AT, Oda T, Purnomo CW, Kashiwagi T, Aziz M. Liquid hydrogen, methylcyclohexane, and ammonia as potential hydrogen storage: Comparison review. *Int J Hydrogen Energy* 2019;44:15026–44.
- Moradi R, Groth KM. Hydrogen storage and delivery: review of the state of the art technologies and risk and reliability analysis. *Int J Hydrogen Energy* 2019;44: 12254–69.
- Demirci UB, Miele P. Chemical hydrogen storage: ‘material’ gravimetric capacity versus ‘system’ gravimetric capacity. *Energy Environ Sci* 2011;4:3334–41.
- Chen Z, Kirlikovali KO, Idrees KB, Wasson MC, Farha OK. Porous materials for hydrogen storage. *Chem* 2022.
- Zhao D, Wang X, Yue L, He Y, Chen B. Porous metal-organic frameworks for hydrogen storage. *Chem Commun* 2022.
- Kopac T. Covalent organic frameworks-based nanomaterials for hydrogen storage. *Covalent Organic Frameworks* 2022;345–60.
- Langmi HW, McGrady GS. Non-hydride systems of the main group elements as hydrogen storage materials. *Coord Chem Rev* 2007;251:925–35.
- Mohan M, Sharma VK, Kumar EA, Gayathri V. Hydrogen storage in carbon materials—a review. *Energy Stor.* 2019;1:e35.
- Camp J, Stavila V, Allendorf MD, Prendergast D, Haranczyk M. Critical factors in computational characterization of hydrogen storage in metal–organic frameworks. *J Phys Chem C* 2018;122:18957–67.
- Aziz M, Wijayanta AT, Nandiyanto ABD. Ammonia as effective hydrogen storage: a review on production, storage and utilization. *Energies* 2020;13:3062.
- Amin AM, Croiset E, Epling W. Review of methane catalytic cracking for hydrogen production. *Int J Hydrogen Energy* 2011;36:2904–35.
- Li H, Yang Q, Chen X, Shore SG. Ammonia borane, past as prolog. *J Organomet Chem* 2014;751:60–6.
- Bartoli M, Pirri CF, Bocchini S. Unraveling the effect of carbon nanotube oxidation on solid-state decomposition of ammonia borane/carbon nanotube composites. *J Phys Chem C* 2022;126:7.
- Ahluwalia R, Peng J, Hua T. Hydrogen release from ammonia borane dissolved in an ionic liquid. *Int J Hydrogen Energy* 2011;36:15689–97.
- Nakagawa T, Burrell AK, Del Sesto RE, Janicke MT, Nekimkin AL, Purdy GM, Paik B, Zhong R-Q, Semelsberger TA, Davis BL. Physical, structural, and dehydrogenation properties of ammonia borane in ionic liquids. *RSC Adv* 2014;4: 21681–7.
- Valero-Pedraza MJ, Martín-Cortés A, Navarrete A, Bernejo MD, Martín Á. Kinetics of hydrogen release from dissolutions of ammonia borane in different ionic liquids. *Energy* 2015;91:742–50.
- Balla Á, Nagyházi M, Turczel G, Solt HE, Mihályi MR, Hancsók J, Vályon J, Nagy T, Kéki S, Anastas PT. Hydrolytic dehydrogenation of ammonia borane in neat water using recyclable zeolite-supported cyclic alkyl amino carbene (CAAC)–Ru catalysts. *New J Chem* 2022;46:16309–16.
- Pei Y, Niu Y, Zhang W, Zhang Y, Ma J, Li Z. Ionic liquid microemulsion mediated synthesis of Pt/TiO<sub>2</sub> nanocomposites for ammonia borane hydrolysis. *Int J Hydrogen Energy* 2022;47:2819–31.
- Meng Y, Sun Q, Zhang T, Zhang J, Dong Z, Ma Y, Wu Z, Wang H, Bao X, Sun Q. Cobalt-promoted noble-metal catalysts for efficient hydrogen generation from ammonia borane hydrolysis. *J Am Chem Soc* 2023;145:5486–95.
- Gong B, Wu H, Sheng L, Zhang W, Wu X. Hydrolysis of ammonia borane on a single Pt atom supported by N-doped graphene. *ACS Appl Mater Interfaces* 2022;14: 13231–9.
- Guo A, Hu L, Peng Y, Wang Y, Long Y, Fu J, Fan G. Steam pretreatment-mediated catalytic activity modulation for ammonia borane hydrolysis over ruthenium nanoclusters on nitrogen/oxygen-rich carbon nanotubes. *Appl Surf Sci* 2022;579: 152158.
- Feng K, Zhong J, Zhao B, Zhang H, Xu L, Sun X, Lee ST. Cu<sub>x</sub>Co<sub>1-x</sub>O nanoparticles on graphene oxide as a synergistic catalyst for high-efficiency hydrolysis of ammonia–borane. *Angew Chem Int Ed* 2016;55:11950–4.
- Barakat NA. Effective Co–Mn–O nanofibers for ammonia borane hydrolysis. *Mater Lett* 2013;106:229–32.
- Özkar S. A review on platinum (0) nanocatalysts for hydrogen generation from the hydrolysis of ammonia borane. *Dalton Trans* 2021;50:12349–64.
- Sun D, Mazumder V, Metin O, Sun S. Catalytic hydrolysis of ammonia borane via cobalt palladium nanoparticles. *ACS Nano* 2011;5:6458–64.
- Ma H, Na C. Isokinetic temperature and size-controlled activation of ruthenium-catalyzed ammonia borane hydrolysis. *ACS Catal* 2015;5:1726–35.
- Wang L, Li H, Zhang W, Zhao X, Qiu J, Li A, Zheng X, Hu Z, Si R, Zeng J. Supported rhodium catalysts for ammonia–borane hydrolysis: dependence of the catalytic activity on the highest occupied state of the single rhodium atoms. *Angew Chem Int Ed* 2017;56:4712–8.
- Zaki AH, Tsunoi N, Ide Y. Controlled synthesis of oxidation-insensitive green rust, a mixed-valent iron mineral, for enhancing solar hydrogen production via hydrolysis of ammonia borane. *ACS Sustainable Chem Eng* 2023;11:2295–302.
- Li J, Sun W, Gao P, An J, Li X, Sun W. Coffee ground derived biochar embedded Ov-NiCoO<sub>2</sub> nanoparticles for efficiently catalyzing a boron-hydrogen bond break. *Sci Total Environ* 2021;761:144192.
- Chu H, Li N, Qiu X, Wang Y, Qiu S, Zeng J-L, Zou Y, Xu F, Sun L. Poly (N-vinyl-2-pyrrolidone)-stabilized ruthenium supported on bamboo leaf-derived porous carbon for NH<sub>3</sub>BH<sub>3</sub> hydrolysis. *Int J Hydrogen Energy* 2019;44:29255–62.
- Dennehy C, Lawlor PG, Jiang Y, Gardiner GE, Xie S, Nghiem LD, Zhan X. Greenhouse gas emissions from different pig manure management techniques: a critical analysis. *Front Environ Sci Eng* 2017;11:1–16.
- Wang Q, Awasthi MK, Zhao J, Ren X, Wang M, Li R, Wang Z, Zhang Z. Utilization of medical stone to improve the composition and quality of dissolved organic matter in composted pig manure. *J Clean Prod* 2018;197:472–8.
- Petersen S, Lind A-M, Sommer S. Nitrogen and organic matter losses during storage of cattle and pig manure. *J Agric Sci* 1998;130:69–79.
- Zhang P, Sun H, Yu L, Sun T. Adsorption and catalytic hydrolysis of carbaryl and atrazine on pig manure-derived biochars: impact of structural properties of biochars. *J Hazard Mater* 2013;244:217–24.
- Ramachandran PV, Gagare PD. Preparation of ammonia borane in high yield and purity, methanolysis, and regeneration. *Inorg Chem* 2007;46:7810–7.
- Tamborrino V, Costamagna G, Bartoli M, Rovere M, Jagdale P, Lavagna L, Ginepro M, Tagliaferro A. Catalytic oxidative desulfurization of pyrolytic oils to fuels over different waste derived carbon-based catalysts. *Fuel* 2021;296:120693.
- Tagliaferro A, Rovere M, Padovano E, Bartoli M, Giorcelli M. Introducing the novel mixed Gaussian-lorentzian lineshape in the analysis of the Raman signal of biochar. *Nanomaterials* 2020;10:1748.

- [46] Torquato LD, Crnkovic PM, Ribeiro CA, Crespi MS. New approach for proximate analysis by thermogravimetry using CO<sub>2</sub> atmosphere: validation and application to different biomasses. *J Therm Anal Calorim* 2017;128:1–14.
- [47] Kathribail AR, Rezaqita A, Lager D, Hamid R, Surace Y, Berecibar M, Van Mierlo J, Hubin A, Jahn M, Kahr J. High-performance amorphous carbon coated LiNiO<sub>2</sub>. *Batteries* 2021;7:69.
- [48] Piatti E, Colangelo M, Bartoli M, Medeiros O, Gonnelli RS, Berggren KK, Daghero D. Reversible tuning of superconductivity in ion-gated NbN ultrathin films by self-encapsulation with a High- $\kappa$  dielectric layer. *Phys Rev Appl* 2022;18:054023.
- [49] Abutaleb A, Zouli N, El-Halwany M, Ubaidullah M, Yousef A. Graphitic nanofibers supported NiMn bimetallic nanoalloys as catalysts for H<sub>2</sub> generation from ammonia borane. *Int J Hydrogen Energy* 2021;46:35248–60.
- [50] Mohajeri N, Ali T, Adebisi O. Hydrolytic cleavage of ammonia-borane complex for hydrogen production. *J Power Sources* 2007;167:482–5.
- [51] Saeys W, Mouazen AM, Ramon H. Potential for onsite and online analysis of pig manure using visible and near infrared reflectance spectroscopy. *Biosyst Eng* 2005;91:393–402.
- [52] Socrates G. Infrared and Raman characteristic group frequencies: tables and charts. third ed. Chichester, U.K.: John Wiley & Sons; 2001.
- [53] Tuinstra F, Koenig JL. Raman spectrum of graphite. *J Chem Phys* 1970;53:1126–30.
- [54] Bartoli M, Giorcelli M, Jagdale P, Rovere M, Tagliaferro A, Chae M, Bressler DC. Shape tunability of carbonized cellulose nanocrystals. *SN Appl Sci* 2019;1:1661.
- [55] Bartoli M, Giorcelli M, Rosso C, Rovere M, Jagdale P, Tagliaferro A. Influence of commercial biochar fillers on brittleness/ductility of epoxy resin composites. *Appl Sci* 2019;9:13.
- [56] Bartoli M, Nasir MA, Passaglia E, Spiniello R, Jagdale P, Rosso C, Giorcelli M, Rovere M, Tagliaferro A. Influence of pyrolytic thermal history on olive pruning biochar and related epoxy composites mechanical properties. *J Compos Mater* 2020;54:1863–73.
- [57] Noori A, Bartoli M, Frache A, Piatti E, Giorcelli M, Tagliaferro A. Development of pressure-responsive PolyPropylene and biochar-based materials. *Micromachines* 2020;11:339.
- [58] Torsello D, Bartoli M, Giorcelli M, Rovere M, Arrigo R, Malucelli G, Tagliaferro A, Ghigo G. High frequency electromagnetic shielding by biochar-based composites. *Nanomaterials* 2021;11:2383.
- [59] Torsello D, Ghigo G, Giorcelli M, Bartoli M, Rovere M, Tagliaferro A. Tuning the microwave electromagnetic properties of biochar-based composites by annealing. *Carbon Trends* 2021;100062.
- [60] Yew YP, Shameli K, Miyake M, Khairudin NBBA, Mohamad SEB, Hara H, Nordin MFBM, Lee KX. An eco-friendly means of biosynthesis of superparamagnetic magnetite nanoparticles via marine polymer. *IEEE Trans Nanotechnol* 2017;16:1047–52.
- [61] Wang H, Hu P, Pan Da, Tian J, Zhang S, Volinsky AA. Carbothermal reduction method for Fe<sub>3</sub>O<sub>4</sub> powder synthesis. *J Alloys Compd* 2010;502:338–40.
- [62] Das B, Reddy M, Chowdari B. Li-storage of Fe<sub>3</sub>O<sub>4</sub>/C composite prepared by one-step carbothermal reduction method. *J Alloys Compd* 2013;565:90–6.
- [63] Liu Y, Li Y, Jiang K, Tong G, Lv T, Wu W. Controllable synthesis of elliptical Fe<sub>3</sub>O<sub>4</sub>@C and Fe<sub>3</sub>O<sub>4</sub>/Fe@C nanorings for plasmon resonance-enhanced microwave absorption. *J Mater Chem C* 2016;4:7316–23.
- [64] Sager M. Trace and nutrient elements in manure, dung and compost samples in Austria. *Soil Biol Biochem* 2007;39:1383–90.
- [65] Kalidindi SB, Indirani M, Jagirdar BR. First row transition metal ion-assisted ammonia–borane hydrolysis for hydrogen generation. *Inorg Chem* 2008;47:7424–9.
- [66] Chen J, Cai H, Zhao T. Solid-state mechanochemical synthesis of Rh/Al<sub>2</sub>O<sub>3</sub> catalysts for effective hydrolysis of ammonia borane. *Mol Catal* 2022;528:112518.
- [67] Lapin N, D'yankova NY. Hydrogen evolution kinetics during transition metal oxide-catalyzed ammonia borane hydrolysis. *Inorg Mater* 2013;49:975–9.
- [68] Meng J, Feng X, Dai Z, Liu X, Wu J, Xu J. Adsorption characteristics of Cu (II) from aqueous solution onto biochar derived from swine manure. *Environ Sci Pollut Control Ser* 2014;21:7035–46.
- [69] Wu H, Cheng Y, Fan Y, Lu X, Li L, Liu B, Li B, Lu S. Metal-catalyzed hydrolysis of ammonia borane: mechanism, catalysts, and challenges. *Int J Hydrogen Energy* 2020;45:30325–40.
- [70] Song J, Wu F, Lu Y, Zhang X. F-doped CeO<sub>2</sub> supported Co-based nanoparticles for enhanced photocatalytic H<sub>2</sub> evolution from ammonia borane. *Int J Hydrogen Energy* 2023;48:13202–12.
- [71] Patra D, Garg R, Gautam UK, Gopalan B. Mitigation of polyborate precipitation on Pd/Fe<sub>2</sub>O<sub>3</sub> sites during ammonia borane hydrolysis: an alternate insight into the role of oxygen vacancies. *Int J Hydrogen Energy* 2023;48:28333–42.
- [72] Aksoy M, Korkut SE, Metin Ö. The rational design of gCN/a-WO<sub>x</sub>/Pt heterostructured nanophotocatalysts for boosting the hydrogen generation from the hydrolysis of ammonia borane under visible light. *Int J Hydrogen Energy* 2023;48:22921–33.
- [73] Wang M, Wang J, Zhao X, Qin G, Zhang X, Lu Z, Yu X, Li L, Yang X. CuCo<sub>2</sub>O<sub>4</sub>–NiO heterostructure catalysts for hydrogen production from ammonia borane. *Int J Hydrogen Energy* 2023;48:19543–53.
- [74] Xu Q, Chandra M. Catalytic activities of non-noble metals for hydrogen generation from aqueous ammonia–borane at room temperature. *J Power Sources* 2006;163:364–70.
- [75] Yan JM, Zhang XB, Han S, Shioyama H, Xu Q. Iron-nanoparticle-catalyzed hydrolytic dehydrogenation of ammonia borane for chemical hydrogen storage. *Angew Chem Int Ed* 2008;47:2287–9.
- [76] Yan J-M, Zhang X-B, Han S, Shioyama H, Xu Q. Synthesis of longtime water/air-stable Ni nanoparticles and their high catalytic activity for hydrolysis of ammonia–borane for hydrogen generation. *Inorg Chem* 2009;48:7389–93.
- [77] Zahmakiran M, Durap F, Özkaz S. Zeolite confined copper (0) nanoclusters as cost-effective and reusable catalyst in hydrogen generation from the hydrolysis of ammonia-borane. *Int J Hydrogen Energy* 2010;35:187–97.
- [78] Chandra M, Xu Q. Room temperature hydrogen generation from aqueous ammonia-borane using noble metal nano-clusters as highly active catalysts. *J Power Sources* 2007;168:135–42.
- [79] Zahmakiran M, Özkaz S. Zeolite framework stabilized rhodium (0) nanoclusters catalyst for the hydrolysis of ammonia-borane in air: outstanding catalytic activity, reusability and lifetime. *Appl Catal B Environ* 2009;89:104–10.